1	Bottom simulating reflections across the northern Gulf of Mexico slope
2	Aditya Kumar ^a , Ann E. Cook ^a , Alexey Portnov ^b , Stuart Skopec ^c , Matthew Frye ^d , Stephen Palmes ^d
3	^a School of Earth Sciences, The Ohio State University, Columbus, OH, USA
4	^b Instituto Andaluz de Ciencias de la Tierra, CSIC-Universidad de Granada, Granada, Spain
5	^c Battelle, Columbus, OH, USA
6	^d Bureau of Ocean Energy Management, Sterling, VA, USA
7	
8	Keywords: bottom simulating reflection, gas hydrate, Gulf of Mexico
9	
10	
11	
12	
13	
14	
15	
16	
17	

Abstract

19

20

21

22

23

24

25

26

27

28

29

30

31

32

33

34

35

36

37

Bottom simulating reflections (BSRs) are widely used indicators for natural gas hydrate in reflection seismic data. BSRs, however, are typically studied on a local scale at a single site and less frequently on a large, regional scale. Herein, we map and describe BSRs over a 68,000 km² area across the northern Gulf of Mexico slope, using publicly released industry-acquired 3D seismic data. We map 74 BSR zones that cover a total area of 2060 km². To understand the characteristics of these BSR zones, we classify them based on their BSR characteristics in the seismic data (continuous, discontinuous, and clustered) and the geological settings in which they appear (structural, stratigraphic, and venting). The most common type of BSRs are discontinuous BSRs; such BSRs were mapped over ~60% of the total BSR area. Discontinuous BSRs occur most commonly in structural or stratigraphic settings. Discontinuous BSRs indicate that gas and hydrate are likely concentrated in discrete layers crossing the base of the hydrate stability zone (HSZ). Continuous BSRs occur in 27% of the total BSR area and they primarily occur in venting and stratigraphic settings. At vent sites, hydrate formation likely reduces sediment permeability and focuses fluid flow laterally underneath the base of the HSZ, likely resulting in a continuous BSR along the area of lateral gas flow. Clustered BSRs, chaotic sequences of high amplitude reflections, occur in only 13% of the total BSR area and are only found within structural settings. In addition, the majority of clustered BSR zones are close to paleochannels, suggesting that clustered BSRs may be more common where coarser-grained sediments exist.

38

39

1. Introduction

41

Natural gas hydrate, a solid clathrate of methane and water, occurs across the Gulf of Mexico slope 42 43 in a variety of geological settings (Brooks et al., 1986; Majumdar et al., 2017; Shedd et al., 2012). 44 Gas hydrates are important for a number of reasons: hydrates may cause submarine slope failure or overpressure in wells (Maslin et al., 2004; McIver, 1982), they could be a natural gas resource 45 46 (Boswell and Collett, 2011; Frye, 2008), and they are a large, but poorly constrained component of the global carbon cycle (Dickens, 2003; Shakhova et al., 2014; Wallmann et al., 2012). 47 In seismic data, the presence of gas hydrate in marine sediments is inferred from BSRs, which are 48 non-stratigraphic seismic reflections with polarity opposite of the seafloor. BSRs are usually 49 parallel to the seafloor and may crosscut geological layers (Hillman et al., 2017b; Hyndman and 50 Spence, 1992). A BSR marks the thermodynamic boundary below which gas hydrate is not stable 51 due to the increase in temperature; the BSR depth is usually equivalent to the thermodynamic base 52 of the hydrate stability zone (HSZ) (Hyndman and Spence, 1992; Villinger et al., 2010). The 53 54 presence of gas below the HSZ lowers the bulk moduli of the sediments (Petersen et al., 2007). A number of sedimentary systems with BSRs have been identified throughout the northern Gulf 55 of Mexico (Boswell et al., 2012; Portnov et al., 2020; Shedd et al., 2012). Most previous research 56 57 focuses on a single gas hydrate system in detail. Typically, each of these studies describes the characteristics of the BSRs and potential gas hydrate occurrence within the local geologic 58 environment (e.g. single mini-basin or channel-levee complex) (Hillman et al., 2017b; McConnell 59 and Kendall, 2002; Portnov et al., 2019, 2021; Snyder et al., 2004). Site specific studies, however, 60 do not provide a clear picture of the influence of different geological settings on gas hydrate 61 systems across the Gulf of Mexico. Herein, we use publicly available 3D multi-channel seismic 62 data (Triezenberg et al., 2016) covering an area of 68,000 km² (Figure 1) in the northern Gulf of 63

Mexico to identify and characterize BSR systems. Mapping BSR systems over such a vast and geologically diverse region, which includes salt tectonics, turbidite channel levee deposits, extensive fault systems, and mud volcanos, allows us to understand the nature of BSRs in a variety of geologic settings. We combine these newly mapped BSR systems with previously mapped BSRs in the Gulf of Mexico: Green Canyon Block-955 (Haines et al., 2017, 2014; Santra et al., 2020), Moby-Dick (Portnov et al., 2021), Orca Basin (Hillman et al., 2017b), Terrebonne (Hillman et al., 2017b; McConnell and Kendall, 2002; Varona et al., 2023), Perdido (Portnov et al., 2022), Jackalope (Portnov et al., 2020), and fifty BSR locations reported but largely undescribed by Shedd et al. (2012). We use this new map of BSR systems to understand the distribution, location and size of BSRs across the northern Gulf of Mexico.

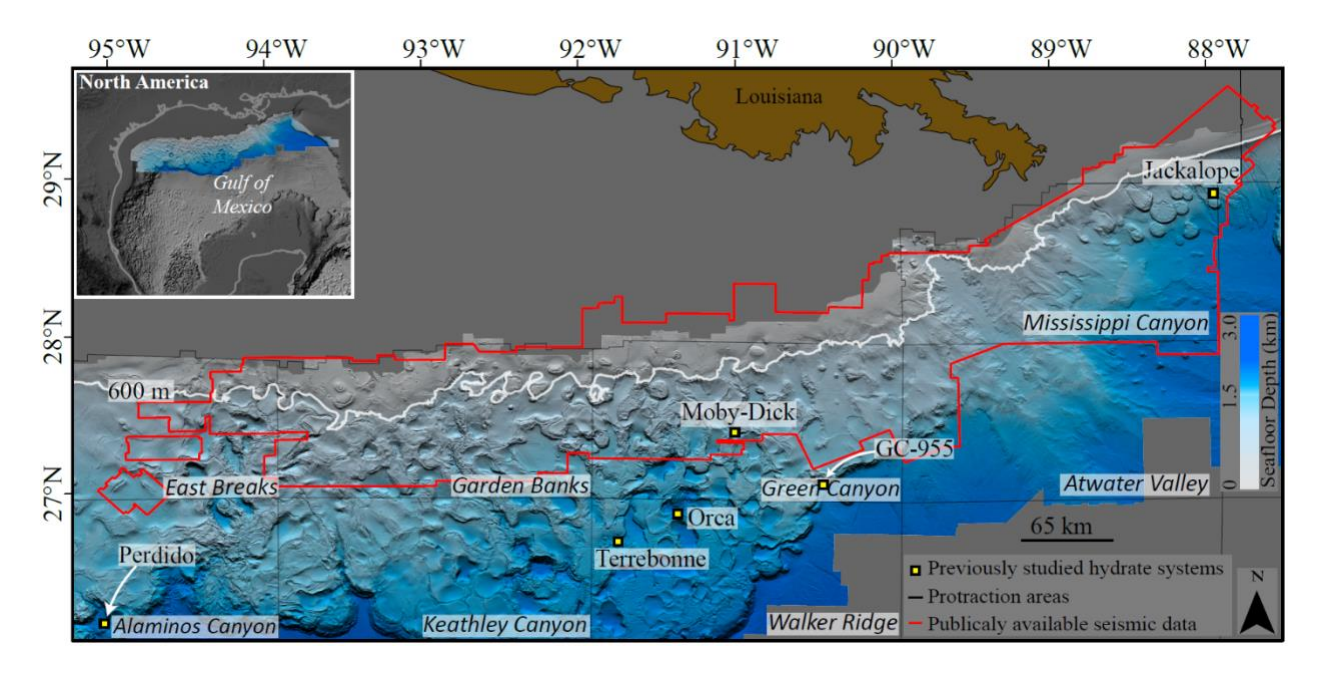


Figure 1: The bathymetry of the northern Gulf of Mexico slope (Kramer and Shedd, 2017) and the protraction areas. A solid white line represents the approximate updip edge of the hydrate stability zone in the Gulf of Mexico at 600 m water depth. Red polygons outline the boundary of the publicly

available seismic data used in this study (Triezenberg et al., 2016). Yellow squares indicate previously studied gas-hydrate locations in the northern Gulf of Mexico.

1.1 Gulf of Mexico geological setting

78

79

80

81

82

83

84

85

86

87

88

89

90

91

92

93

94

95

96

97

98

99

100

The Gulf of Mexico formed during the Late Triassic rifting event separating North America from South America (Galloway, 2008; Salvador, 1991). The tensional deformation due to rifting resulted in the formation of regional features such as extensional faults, grabens, and half grabens (Salvador, 1991). During the Middle Jurassic period, the restricted connectivity of the Gulf of Mexico with the surrounding ocean led to the deposition of a 2000-3000 m thick layer of salt in the Texas-Louisiana slope region (Weimer et al., 2017). During the Cenozoic period, rapid siliciclastic sediment deposition over these salt layers resulted in salt mobilization causing the formation of minibasins and salt-cored structures (Figure 1) (Galloway, 2008; Weimer et al., 2017). Minibasins are localized depressions of tens to hundreds of square kilometers formed by the gravitational subsidence of overlying sediments caused by the movement of subsurface salt. Regional tectonic activity and progradation of river deltas during the Miocene-Pleistocene epoch, resulted in increased turbidite deposition (Galloway, 2008; Roesink et al., 2004). Sand-filled turbidite channel systems with well-developed levees and slope fan facies are commonly observed (Galloway, 2008; Roesink et al., 2004). Natural gas hydrate is observed across the Gulf of Mexico slope in a variety of lithofacies and geological settings: within turbidite sediments (Flemings et al., 2020; Portnov et al., 2019), channel levees (Frye et al., 2012; Santra et al., 2020), structural and stratigraphic traps (Hillman et al., 2017a; Simonetti et al., 2013), close to vents and seeps (Roberts et al., 2006), over salt ridges (Milkov and Sassen, 2001), and within minibasins (Milkov and Sassen, 2001). Scientific ocean drilling holes in the northern Gulf of Mexico slope show shallow, near seafloor sediments in the

gas hydrate stability zone are of Pleistocene age and primarily composed of clay, mud, and fine sands (deepest penetrated depth is ~299 m) (Expedition 308 Scientists, 2006a, 2006b; Shipboard Scientific Party, 1986a, 1986b, 1986c).

Salt deformation facilitates the formation of faults and fractures within overlying sediment, which allows vertical fluid migration from deeper petroleum systems to near seafloor sediments. Milkov and Sassen (2001) suggested that focused fluid migration through fault systems associated with salt structures may result in an increased thermogenic gas supply in shallow sediments.

Strata within minibasins, on the other hand, is less deformed than sediments overlying shallow salt bodies; therefore, minibasins typically lack structural-assisted fluid flow pathways for upward transport of deeper hydrocarbons (Sassen et al., 2004). However, hydrate can still form in these systems, as methane gas can be generated from organic matter within shallow sediments and form low concentrations of hydrate. Minibasins, therefore, are likely more favorable for hosting microbial hydrates (Milkov and Sassen, 2001; Sassen et al., 2004).

2. Data and Methods

2.1 3D seismic data

Time-migrated 3D multichannel post-stack seismic reflection data were obtained from the National Archive of Marine Seismic Surveys (NAMSS); these data collected by petroleum companies becomes publicly available after a 25-year moratorium. The data spans a large area across the northern Gulf of Mexico including the protraction areas of East Breaks (EB), Garden Banks (GB), Green Canyon (GC), Mississippi Canyon (MC), and Atwater Valley (AT) (Figure 1). We use fifty-six 3D seismic volumes with a dominant frequency between 20 and 50 Hz (Table S1). The vertical resolution of the data ranges between 10-23 m, using average velocity of 1800 m/s

for near seafloor sediment. Additional details about the acquisition layout for each survey are provided in Supplementary Table S1.

Because acquisition and processing of seismic data were performed using different configurations and protocols, each seismic volume can have different amplitude ranges and polarity. Amplitude normalization was performed to bring all 3D volumes to the same amplitude range. In addition, all the seismic data were converted to zero-phase American polarity, where an increase in acoustic impedance corresponds to a peak-leading seismic reflection (e.g. Boswell et al., 2016).

2.2 Root mean square amplitude analysis

Seismic attribute analysis can help identify the spatial extent of subsurface features that may not be evident when examining seismic amplitude data alone. The root mean square (RMS) amplitude attribute can help emphasize anomalous amplitude zones (Anees et al., 2019; Santra et al., 2020), such as BSRs (Portnov et al., 2020), bright spots (Böttner et al., 2020), and acoustic chimneys (Bünz et al., 2012). We use the RMS amplitude attribute to identify paleochannels and BSRs (Sylvester et al., 2012).

BSRs generally follow the seafloor topography and exhibit strong trough-leading amplitudes (Hyndman and Spence, 1992). We calculate the RMS attribute within several subseafloor depth windows that target predicted depths of HSZ in each area (Figure 2a). To do this, we apply shifts to mapped seafloor surface to better display amplitude anomalies. We estimate a range of depths for the HSZ using the CSMHYD program (Holder et al., 1987; Sloan Jr. and Koh, 2007). For each area, we use the water depth, a geothermal gradient range between 25-55 °C, a pore water salinity

of 3.5%, and 100% methane gas. We use RMS windows between 140 ms and 400 ms, which is

wide enough to capture BSRs even if the estimates for the base of the HSZ are inexact (e.g. due to

local unaccounted variations in geothermal heat flux). Figure 2b shows the RMS amplitudes calculated along a seafloor-parallel surface shifted 350 ms below the seafloor with a search window of 140 ms (70 ms on either side of the reference surface). Windows may contain amplitudes related to features other than BSRs, such as free gas below the HSZ, salt deformation, or carbonates. Therefore, each high RMS amplitude zone is independently verified and further mapped manually in the seismic data. Figure 2c shows an arbitrary seismic cross-section across the high amplitude Zone-13 (see Figure 2b), revealing a discontinuous BSR across the profile and paleochannel signatures.

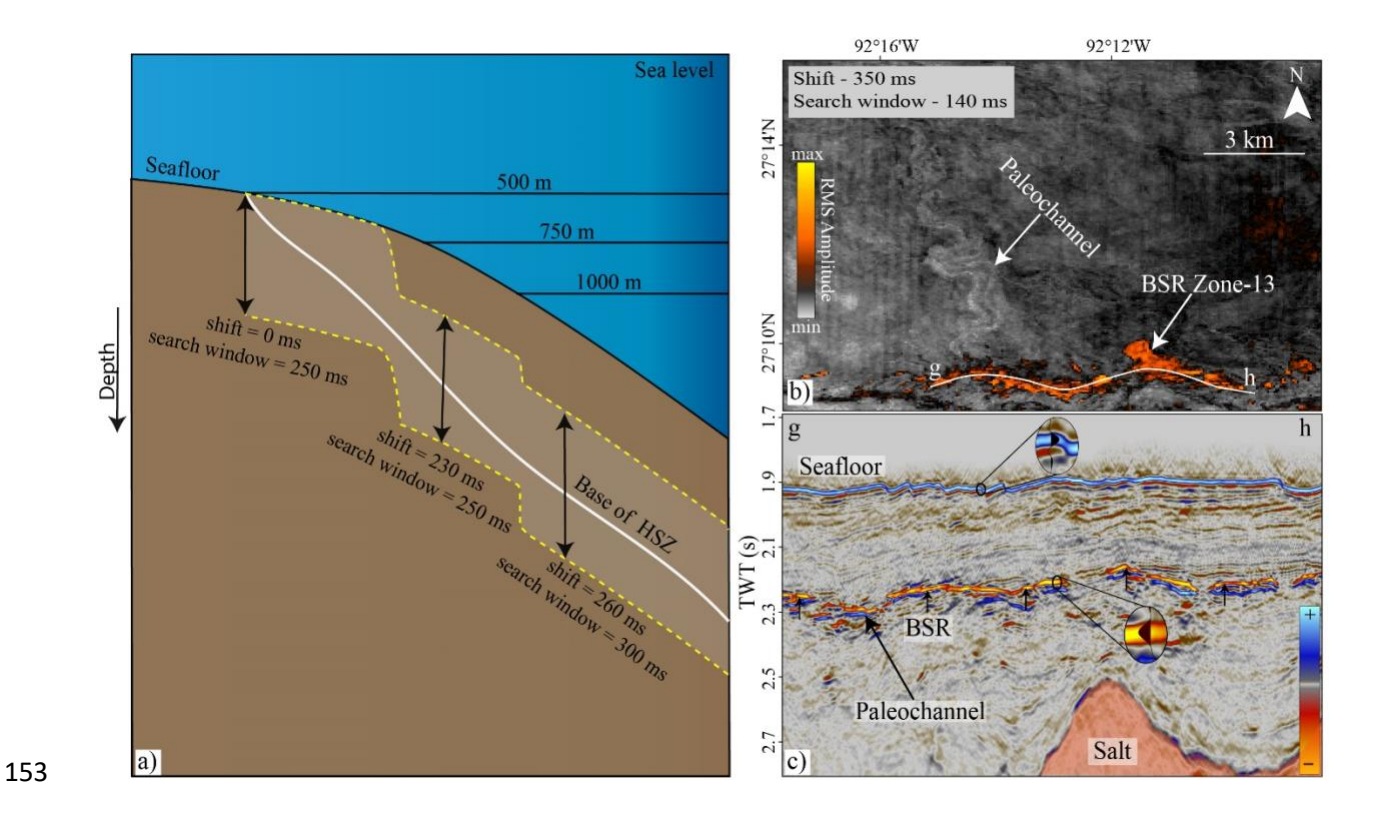


Figure 2: a) BSR were mapped using the RMS amplitude attribute within floating windows (shaded zone) that target the approximate interval of HSZ base in each area. b) Map view of extracted RMS amplitudes within the search window show paleochannels and BSR zones. c) Seismic line gh (Figure 2b) over the identified BSR zone. Shoaling of salt is observed underneath the BSR and

- likely affects the base of hydrate stability. RMS = root mean squared; HSZ= hydrate stability zone;
- TWT = two-way time.

2.3 BSR classification

- Herein, we study BSR systems in terms of their seismic characteristics and geological setting, as
- the type of BSRs may be linked to specific geological settings.
- In this study we classify BSRs by their seismic morphology (continuous, discontinuous and
- clustered), by the geological setting in which they occur (stratigraphic, venting and structural), and
- by the size of the BSR systems.

2.3.1 BSR types (continuous, discontinuous, and clustered)

Continuous BSRs (Figure 3a) are coherent and continuous reflections usually following the seafloor topography and crosscutting seismic reflectors (Hillman et al., 2017b; Shedd et al., 2012; Shipley, 1979; Vanneste et al., 2001). Discontinuous BSRs (Figure 3b), also known as patchy BSRs, are segmented non-coherent lateral reflections that generally follow the seafloor topography (Hillman et al., 2017b; Leslie and Mann, 2022; Shedd et al., 2012). Clustered BSRs (Figure 3c) are a vertical stack of high amplitude reflections within a dome or anticlinal structure with the top reflection roughly parallel to the seafloor (Portnov et al., 2019). This stack of high amplitude reflections indicates the accumulation of free gas in discrete layers below the base of HSZ. Similar clustered BSR systems were described before they were designated as clustered: GC-955 in the Gulf of Mexico (McConnell et al., 2010), ODP Site 995 at Blake Ridge (Hornbach et al., 2008) and off SW Taiwan (Berndt et al., 2019). In this study, the area covered by each BSR type within a BSR zone is interpreted based on the character of the BSR in the seismic data. The seismic profile in Figure 4 shows how the BSR character can change within a single BSR zone. The BSR in the

left of the seismic profile has a dominant, single continuous negative amplitude and this area is designated as a continuous BSR. In the middle there are a number of high-amplitude stacked reflections, and so, this area is identified as a clustered BSR. Finally, the BSR on the right side of the seismic profile again changes to a dominant negative amplitude, however, this amplitude is patchy and not continuous; we, therefore, designate this area as a discontinuous BSR. The inset in Figure 4 shows the area assigned to different BSR types. This exercise is repeated in all BSR zones to qualitatively determine the area of each BSR type (Table S2).

It is important to note that the horizontal resolution of seismic data affects BSR appearance (Hillman et al., 2017b; Vanneste et al., 2001). The horizontal resolution of 3D seismic data is a function of the Fresnel Zone, and it defines the minimal lateral extent of an object or distance between the objects that can be resolved in the seismic image. A shorter wavelength results in a smaller Fresnel Zone, which has a finer lateral resolution and a decrease in the continuity of BSRs (Lindsey, 1989). A continuous BSR with a higher wavelength may appear discontinuous or even disappear in very short wavelength datasets (Vanneste et al., 2001). Seismic wavelength is a function of velocity and frequency; in our case, the velocity of the near-seafloor sedimentary environment is similar and seismic volumes have similar dominant frequencies, from 20-50 Hz (Table S1). Thus, the seismic wavelength is not a significant variable in the classification of BSR type.

2.3.2 Geological setting

BSRs in structural settings coincide with features such as faulting, fracturing, and salt-related deformation (Figure 5a). Milkov and Sassen (2002) were among the first to show that concentrated gas hydrate accumulations occur in structural settings created by salt deformation and faulting. Areas in BSR zones with these features were identified as structural. We define a venting system

as a zone with chimney or vent features or significant acoustic blanking as shown in Figure 5b. In the Gulf of Mexico, gas hydrate can form near vent features both in the subsurface and at the seafloor (Chun et al., 2022; Neurauter and Bryant, 1990; Paull et al., 1991). BSRs in venting settings are adjacent to chimney or blanking features and often form circular or semi-circular shapes around them. Areas with these features and adjacent to these features are characterized as venting settings. Finally, in stratigraphic settings, BSRs occur without clear venting and structural control (Figure 5c). Gas hydrates in these settings may either form due to local microbial methanogenesis (Malinverno, 2010; Malinverno and Goldberg, 2015), fluid flow through permeable layers and/or in faults or fractures not visible on seismic data (Boswell et al., 2012; Milkov and Sassen, 2002). The geologic settings within each BSR zone are selected by analyzing the seismic data and identifying the boundaries between geologic setting.

2.3.3 BSR size

Finally, we classify BSR zones based on their size. BSR zones with an area less than 13 km² are classified as small, 13-30 km² are classified as medium, >30-100 km² are classified as large, and an area of more than 100 km² are classified as extra-large.

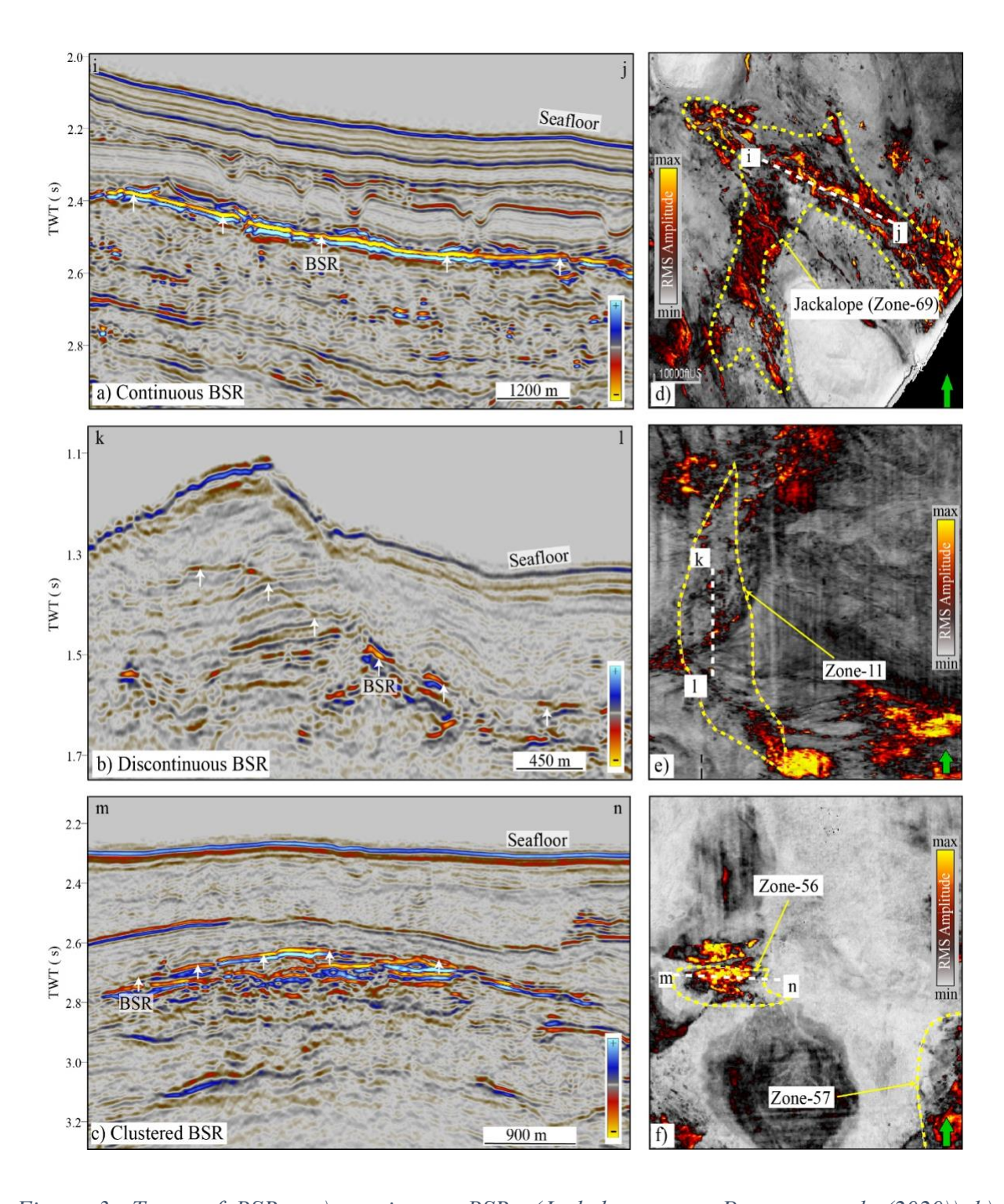


Figure 3: Types of BSRs: a) continuous BSRs (Jackalope zone, Portnov et al. (2020)) b) discontinuous BSRs (Zone-11) c) clustered BSRs (Zone-56). White arrows indicate the BSR. The locations of these seismic profiles are shown with white dotted lines over the RMS amplitude map in d), e), and f), respectively. See Figure 6 for locations of zones.

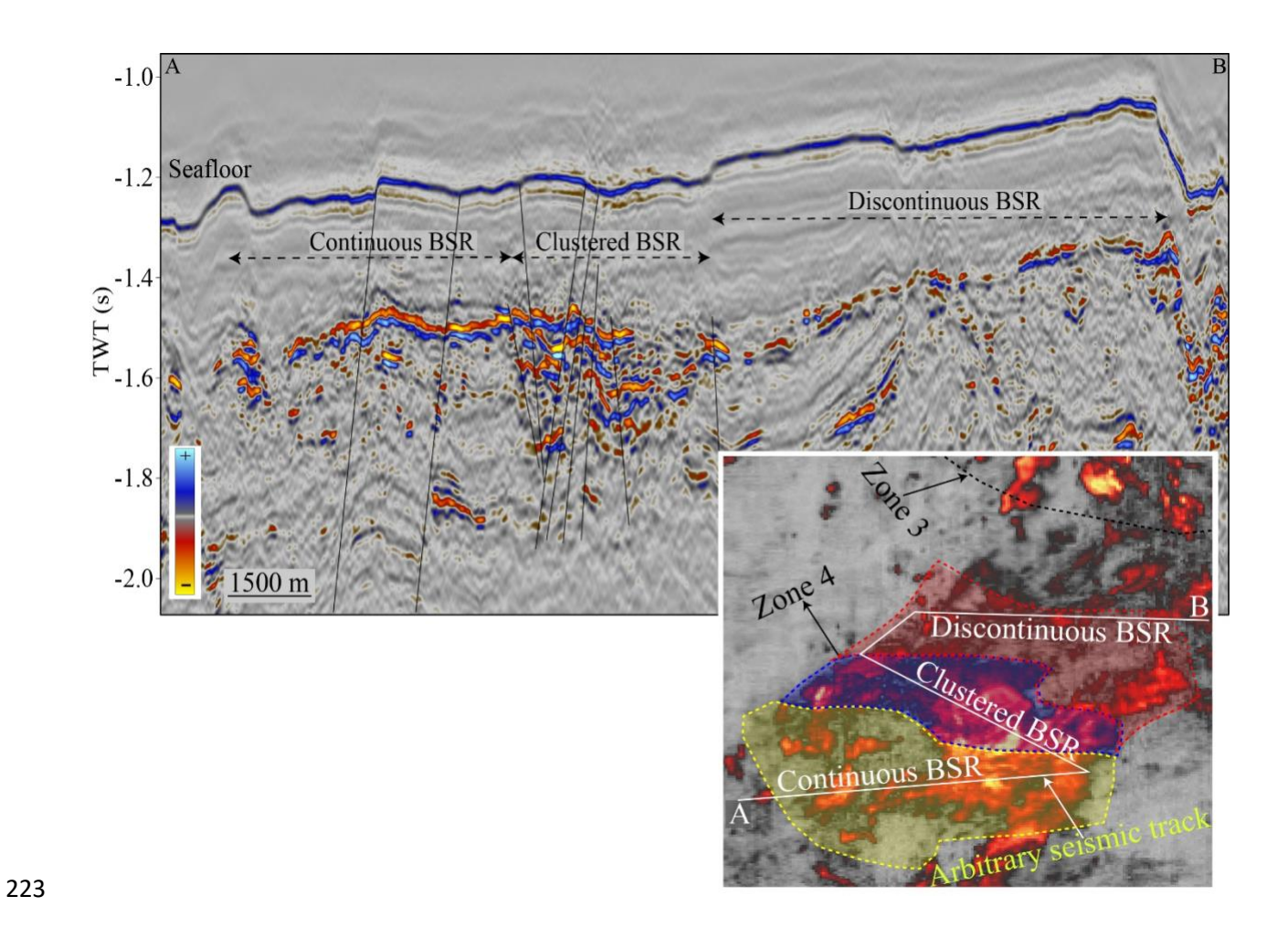


Figure 4: BSR Zone-4 shows multiple BSR types within the same system. The inset shows BSR Zone-4 with arbitrary seismic line AB (white line). The seismic profile across this track has a combination of continuous, clustered, and discontinuous BSRs. The location of Zone 4 is shown in Figure 6e.

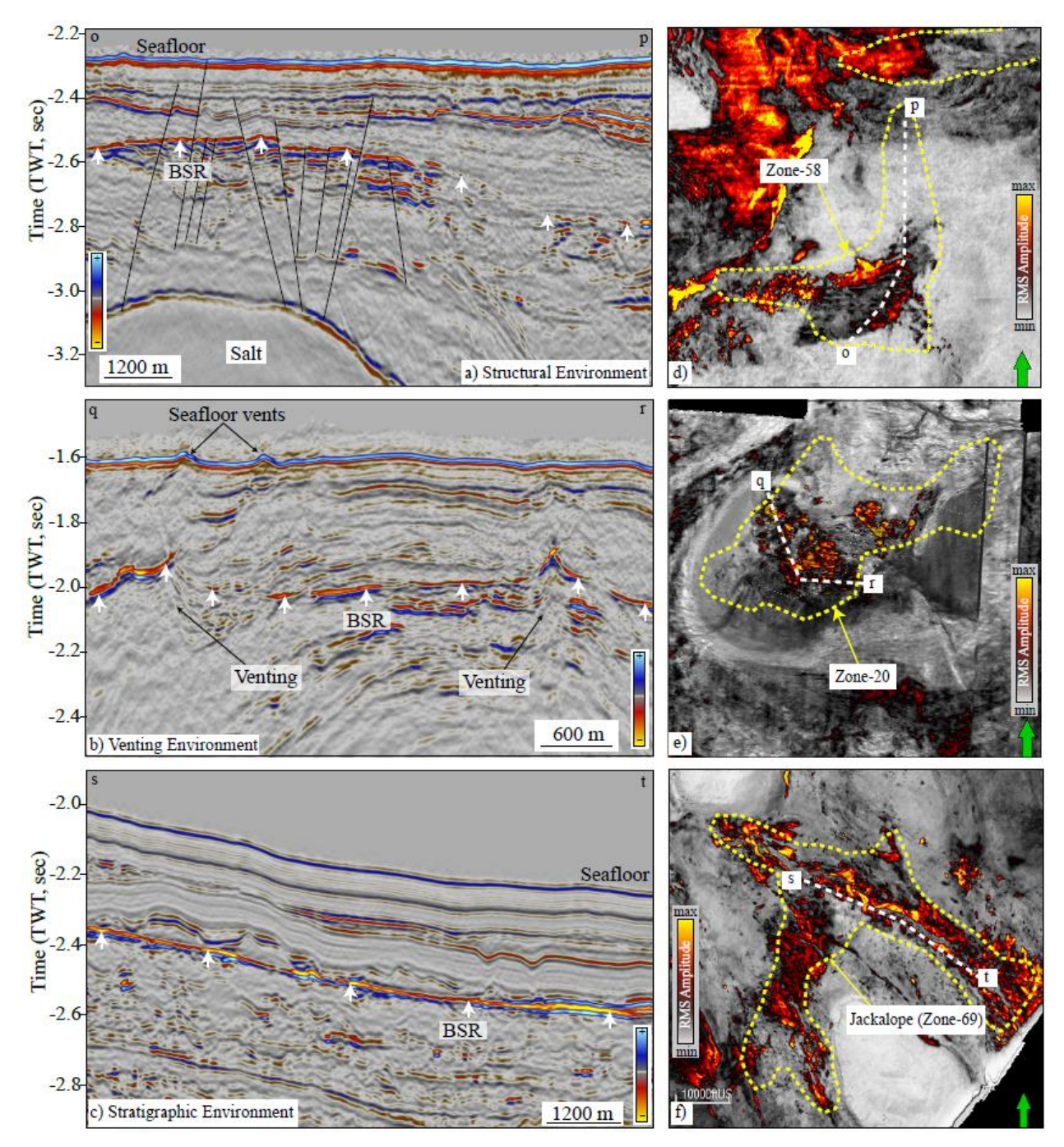


Figure 5: Different geological settings hosting BSRs: a) a structural setting (Zone-58), b) a venting setting (Zone-20), and c) a stratigraphic setting (Jackalope zone (Zone-69), Portnov et al. (2020)). The locations of these seismic profiles are shown with white dotted lines over the RMS amplitude map in d), e), and f), respectively. See Figure 6 for locations of zones.

3. Results and discussion

235

236

237

238

239

240

241

242

243

244

245

246

247

248

249

250

251

252

253

254

255

3.1 Spatial distribution of BSR zones

We evaluate the spatial distribution of 70 BSR zones (Z-1 to Z-70) over the 68,000 km² study area in the northern Gulf of Mexico. Six zones are in the East Breaks protraction area (Z-1 to Z-6), nine zones are in Garden Banks (Z-7 to Z-15), twenty zones are in Green Canyon (Z-16 to Z-35), five zones are in Atwater Valley (Z-36 to Z-40), and thirty zones are in Mississippi Canyon (Z-41 to Z-70) (Figure 1 & Figure 6, Table S2). Eighteen new BSR zones are described in this study: Z-3, 4, 6, 13, 16, 21, 27, 35, 36, 51-54, 56, 57, 59, 62, and 68. In addition, we describe 51 BSR zones originally identified by the U.S. Bureau of Ocean Energy Management (BOEM) and one BSR zone (Jackalope, Z-69) originally identified by Portnov et al. (2020). We were not able to identify all of the BSR zones previously reported by BOEM; the BOEM BSR dataset was interpreted on newer proprietary data, which could explain the differences in BSR interpretation. We also include four other site-specific studies of BSRs outside our study area in our analysis (74 BSR zones combined; Figures 1, 6 and 8): Perdido (Portnov et al., 2019), Orca (Hillman et al., 2017b), Terrebonne (Haines et al., 2014; Hillman et al., 2017b; McConnell and Kendall, 2002), and GC-955 (Haines et al., 2017, 2014; Santra et al., 2020). In total, all BSR zones combined span an area of about 2,060 km² (Table S2). The sizes of BSRs observed in this study range over three orders of magnitude from 2 km² in Green Canyon (Zone-21) to 277 km² in East Breaks (Zone-5). A total of 27 BSR zones are categorized as small, 24 as medium, 20 as large, and 3 as extra-large.

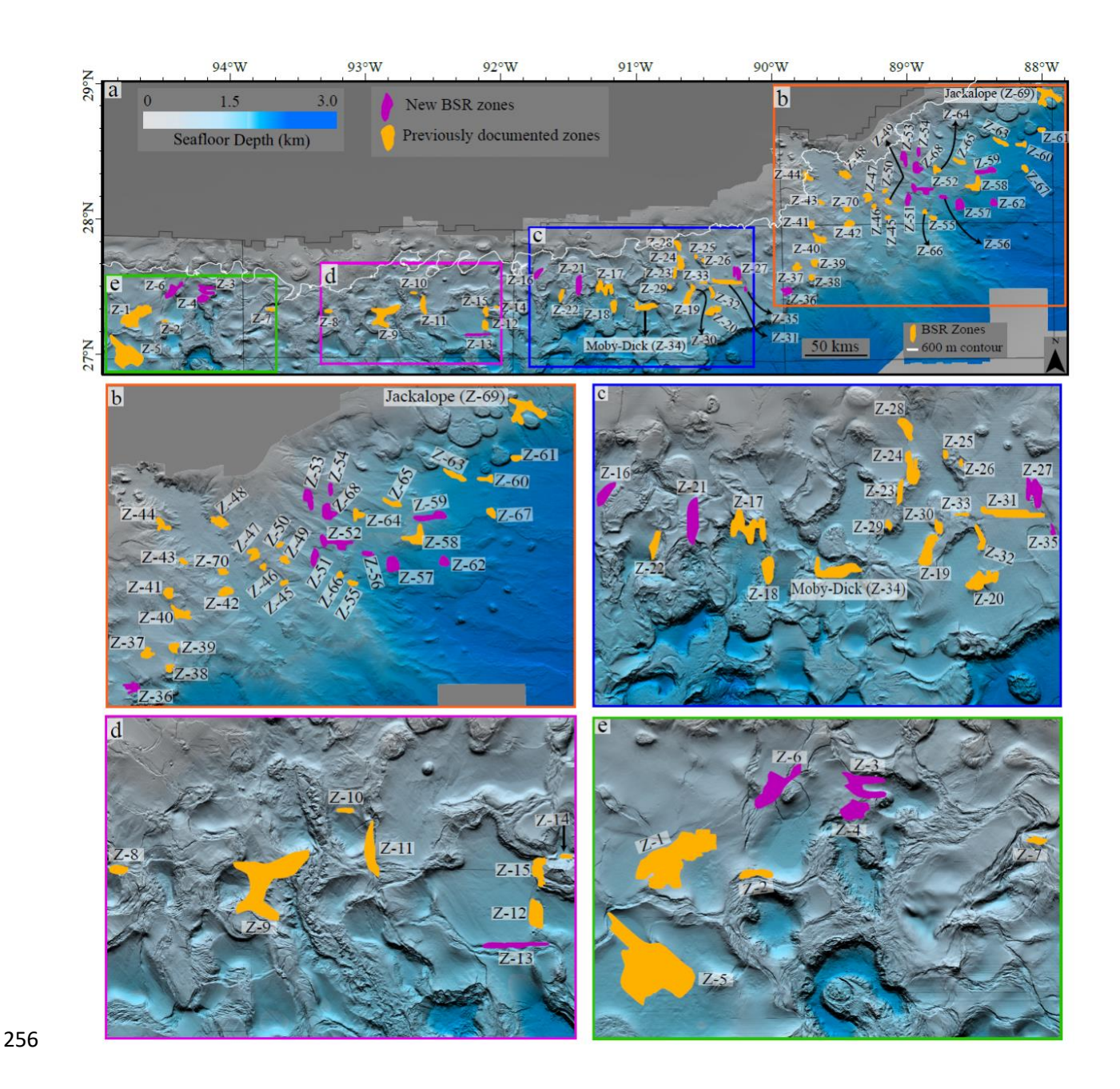


Figure 6: A bathymetric map of the study area showing the spatial distribution of the BSR zones.

Previously documented BSR zones that were confirmed in our study are shown in orange, while zones in magenta are newly identified.

3.2 Geological settings and BSR types

262

263

264

265

266

267

268

269

270

271

272

273

274

275

276

277

278

Hydrate formation and its distribution in the Gulf of Mexico varies in different geological settings (You et al., 2019). In basin-centered and stratigraphic settings, microbial methanogenesis is most likely the primary methane source contributing to hydrate formation (Milkov and Sassen, 2002), while focused flow from deep sources supplies gas to near seafloor sediments in structural (Gullapalli et al., 2019; Sultan et al., 2011) and venting settings (Bünz et al., 2012; Dewangan et al., 2021). Methane recycling at the base of HSZ is another factor that supplies free gas to the HSZ irrespective of geological settings (Nole et al., 2018). In the most common form of this process, the base of HSZ moves up slowly due to sedimentation, causing the dissociation of any hydrate now outside hydrate stability. The free gas released below the HSZ may move up and reenter the HSZ and form hydrate. The most common geological setting for BSR formation is stratigraphic (40% of the total BSR area), followed by structural (39%) and venting (21%) in the Gulf of Mexico. The most common BSR combination occurring together is continuous and discontinuous BSRs, mapped in 20 zones (Figure 7b). Most of the BSR systems (49 zones) occur within a combination of two or three geologic settings; the most common combination is all three geological settings (15 zones) (Figure 7a). An example of a BSR zone with all three types of BSRs is shown in Figure 4.

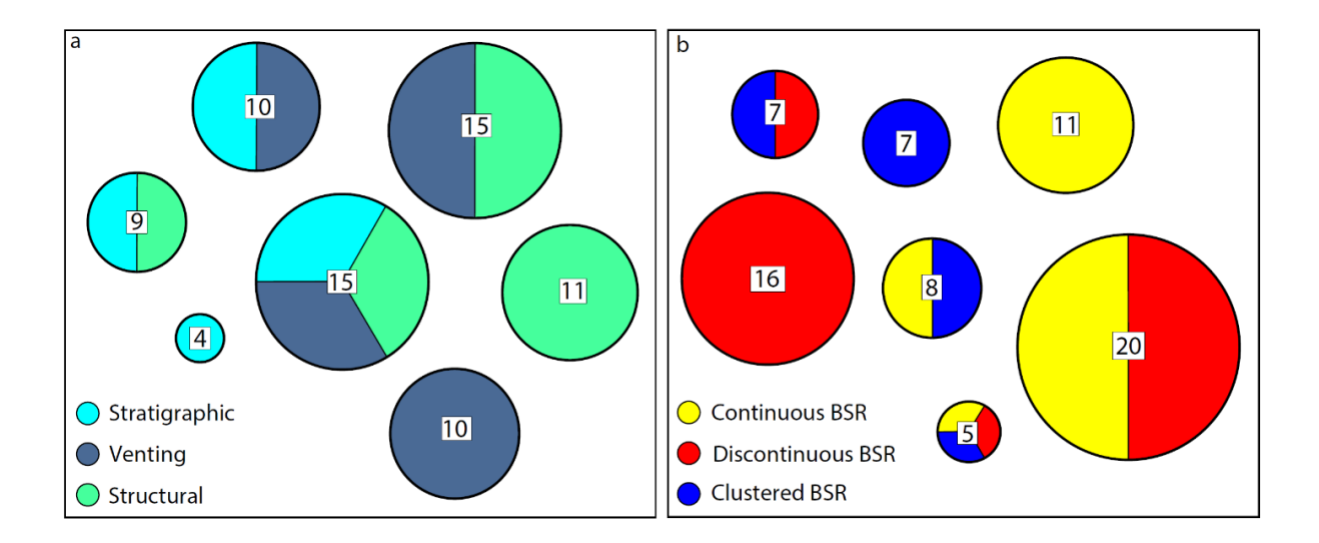


Figure 7: A bubble diagram illustrating the frequency of BSR occurrence a) in combination of different geological settings and b) as combination of different BSR types in the Gulf of Mexico.

The size of the bubbles correspond to the frequency of BSR occurrence.

When considering the total areal extent of each BSR type within the different zones, however, discontinuous BSRs covers almost half (60%) of the total BSR area (Table S2). Continuous and clustered BSRs make up 27% and 13% of the remaining area, respectively.

The prevalence of discontinuous BSRs by overall area and the total number of BSR zones, is likely the result of significant shallow structural deformation in the Gulf of Mexico. In less complex settings, like the contourite sediment deposits of the Blake Ridge on the Atlantic margin (Hillman et al., 2017b; Hornbach et al., 2008; Paull et al., 1996), BSRs are widespread and continuous. Salt tectonic activity in the Gulf of Mexico disrupts the otherwise laterally homogeneous stratification where extensive continuous BSRs are often observed. For example, the shoaling of salt can induce dipping stratigraphy, causing both hydrate and non-hydrate-bearing strata to intersect the base of the hydrate stability zone, thus resulting in the formation of discontinuous BSRs.

3.3 Visualizing BSR type and setting

294

295

296

297

298

299

300

301

302

303

304

305

306

307

308

309

310

311

312

313

314

315

316

We use a ternary diagram to analyze the relationship between BSR type and the geological settings where they occur (Figure 8). The stratigraphic, structural, and venting geologic settings are represented by three axis of the ternary diagram. Each pie chart in the ternary diagram represents one BSR zone. BSR zones comprising a single geological setting are located at the respective vertex, zones combining two geological settings are located at the axis, and zones combining all the geological settings are located inside the ternary diagram. The three BSR types are shown using different colors in a pie chart: yellow for continuous, red for discontinuous, and blue for clustered. The fraction of each color in a pie chart indicates the share of each BSR type in a single BSR zone. Finally, the size of the BSR zone is displayed by the size of the pie chart using following thresholds: small (<10 km²), medium (10-30 km²), large (30-100 km²), and extra-large (> 100 km²). For example, BSR Zone-52 (Figure 8) is represented with a large-sized pie chart indicating it is between 30 and 100 km² in size. The pie chart for Zone-52 represents the fraction of the BSR that is continuous (67%) and discontinuous (33%). All geological settings are observed in Zone-52 (22% structural, 56% venting, and 22% stratigraphic), and thus it appears in the middle of the ternary diagram. Zone-52 is closest to the venting vertex because venting is the most prevalent geologic setting in Zone-52.

3.3.1 Structural settings

Thirty-four BSR zones occur in structural settings (Figure 8); while structural settings host the most BSRs, these BSRs are relatively small in size. In structural settings, the most common BSR types are clustered and discontinuous BSRs (Figure 8). We find that almost all clustered BSRs occur in structural settings which includes Zones-30, 45, 46, 50, 55, 56, 57, 58, 62, 66, 67, Perdido, and GC955.

In structural settings, fault systems that developed due to salt deformation may shuttle free gas and fluids to the HSZ forming highly concentrated gas hydrate (Brooks et al., 1984; Lin et al., 2022; Wei et al., 2022). Alternatively, methane that was once gas hydrate in the HSZ will eventually move below the HSZ due to sediment burial. Below the HSZ, this hydrate will dissociate into water and gas, and the gas can advect back into the HSZ and form highly concentrated gas hydrate near the base of hydrate stability (You et al., 2021). Alternatively, part (or all) of the methane that slowly exited the HSZ during sediment burial could remain in discrete layers below the HSZ and create the conditions that cause a clustered BSR.

In few places where BSRs in structural settings have been drilled in the Gulf of Mexico, high saturation gas hydrates were identified: Tiger Shark (Boswell et al., 2009), Perdido (Portnov et al., 2019), and Green Canyon 955 (Flemings et al., 2020).

3.3.2 Stratigraphic settings

Nineteen BSR zones occur in stratigraphic settings (Figure 8). Stratigraphic settings commonly host both continuous and discontinuous BSR systems (Figure 8). The East Breaks protraction area hosts the two extra-large BSR zones in this study, Zone-1 (171 km²) and Zone-5 (277 km²). These extra-large BSRs significantly contribute to the total area of both stratigraphic settings and discontinuous BSRs, where mean BSR area is 22 km² and 33 km², respectively.

Stratigraphic settings, by our definition, do not have vents or seismically resolvable faults, therefore, it is more likely that methane is generated by in-situ methanogenesis from decomposition of organic matter (Malinverno, 2010; Nole et al., 2017). Moreover, these systems likely have lower concentrations of gas hydrate as previous studies show that microbially

generated hydrate accumulations often have low hydrate concentration (Wallmann et al., 2012; Xu and Ruppel, 1999; You et al., 2019).

In stratigraphic environments, continuous BSRs may be more common where hydrate is distributed in relatively homogeneous sediment, and discontinuous BSRs are more common where hydrate is concentrated in discrete sediment layers that tend to include interbedded sands and marine muds (Figure 9). However, this effect does depend on the orientation of the sedimentary layers relative to the base of the HSZ; if a single gas-bearing layer follows the base of the HSZ over a large area, that area will have a continuous BSR. When a sedimentary system is dipping relative to the base of the HSZ, a discontinuous BSR will occur if gas and hydrate are present in discrete layers intersecting the base of the HSZ (Figure 9).

3.3.3 Venting settings

Twenty-one mapped BSR zones were attributed to the venting settings (Figure 8). In the venting settings, we observe that most of the BSR systems (fifteen out of twenty-one) are continuous BSRs (Zones-2, 10, 12, 14, 20, 22, 26, 40, 41, 47, 49, 52, 54, 61, and 68) (Figure 8). Venting settings in the Gulf of Mexico can have high salinity fluids with elevated temperatures (Milkov et al., 2004; Paull et al., 2005). In some cases, vent systems can exist at three-phase stability between gas, hydrate, and water due to high pore water salinity; this may allow free gas to migrate into hydrate systems (Liu and Flemings, 2007; You et al., 2019). Hydrate formation within and near chimneys can alter the fluid flow behavior, redirecting free gas laterally within and beneath the HSZ, resulting in a continuous BSR along the area of lateral gas flow (Figure 9) (Fraser et al., 2016). Below the HSZ, the lateral extent and rate of methane flow depends on porosity, permeability, and fluid pressure; these factors also control the size of the BSR.

Hydrate systems in venting settings are less common in the Gulf of Mexico and occupy smaller area (20% of total BSR area) than structural (40%) and stratigraphic (40%) settings. Even so, vents can bring high fluxes of fluid/gas into the hydrate stability zone, that may lead to the accumulation of hydrate in high concentrations within and near the vent (Xu and Ruppel, 1999).



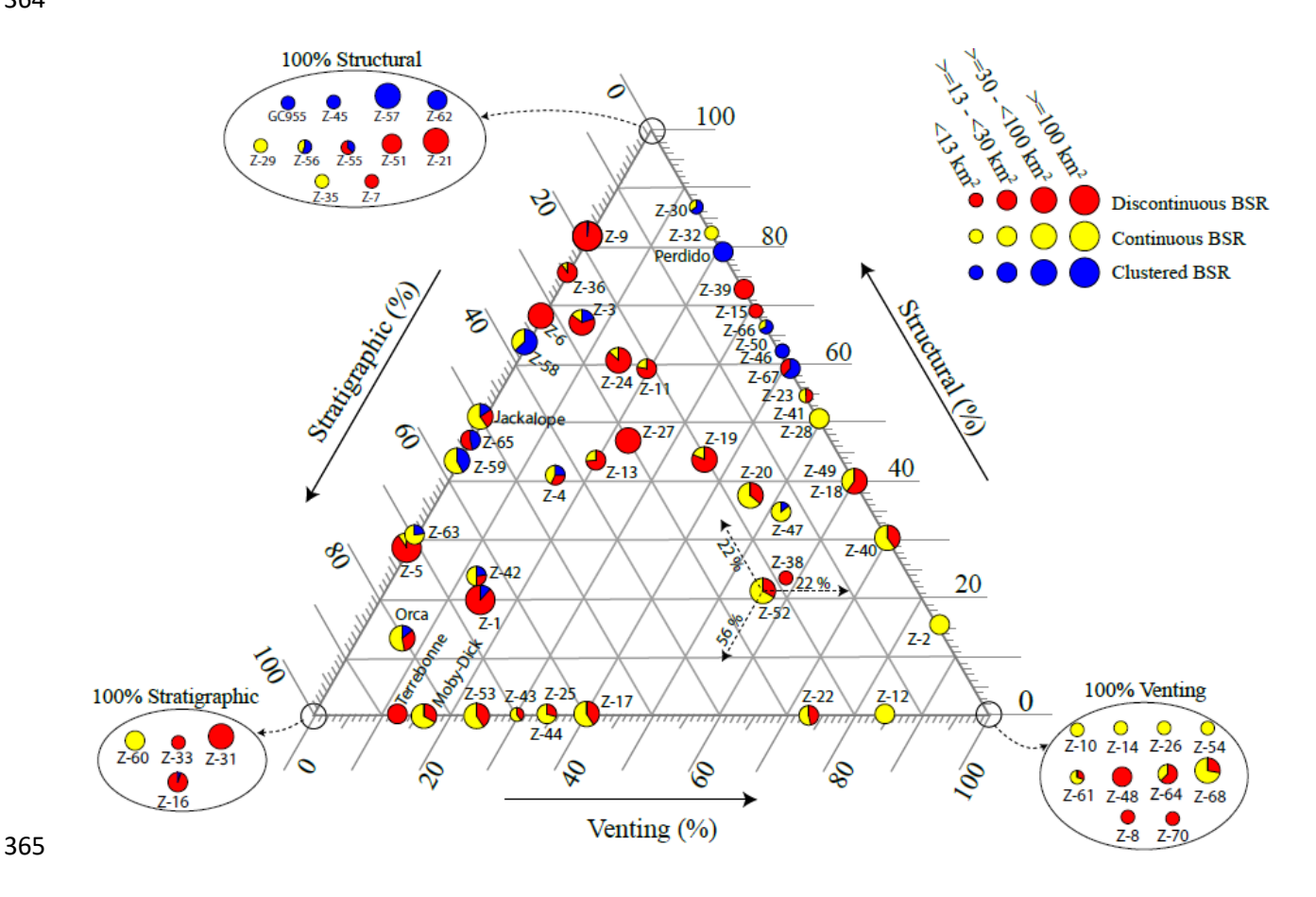


Figure 8: A ternary diagram illustrating the distribution of 74 mapped BSR zones in different geological settings in the Gulf of Mexico. The diagram is interpreted as follows: the axes represent geologic settings, the colors represent the BSR type and the sizes of pie chart indicates relative BSR size. For example, Zone-52 combines all geological settings (22% structural, 56% venting, and 22% stratigraphic); it shows approximately two-third continuous and one-third discontinuous BSR, and it is represented with a large-sized pie chart indicating it is between 30 and 100 km² in

size. Dotted lines with the arrow pointing toward a number on their respective axis represent the percent contribution of respective geological setting in Zone-52. The portion of the colors in the ternary diagram represents percent share of the respective BSR type (In Zone-52, the yellow color represents continuous BSR contribute 67%, and the red color represents discontinuous BSR contribute 33%).

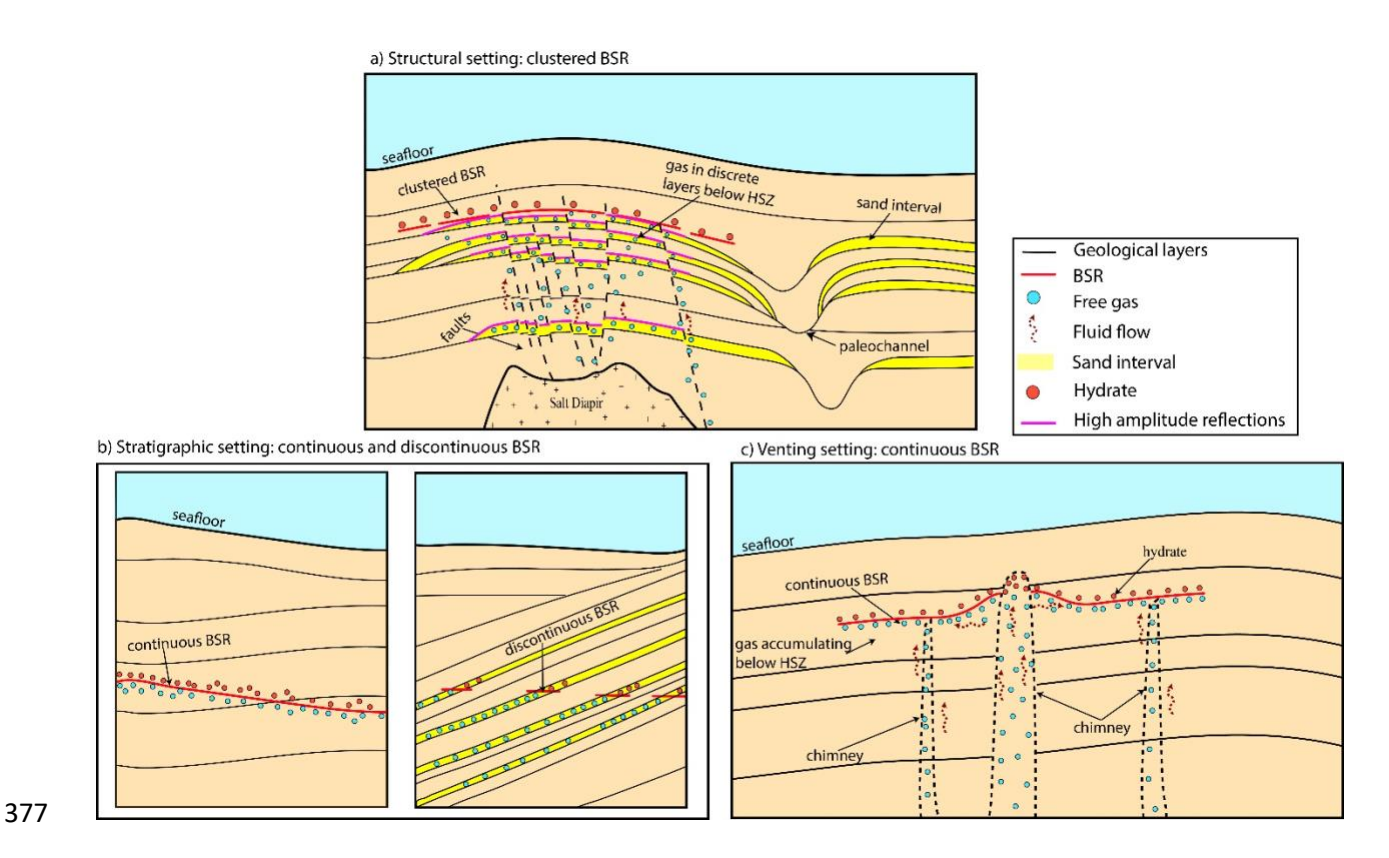


Figure 9: A conceptual diagram illustrating the most common BSRs in each geological setting (structural, stratigraphic, and venting). a) In structural settings, fluid flow is focused through faults and gas accumulates in discrete layers below the base of HSZ that facilitate the formation of clustered BSRs. Clustered BSRs may be more common in paleochannel, sand-rich systems (Yellow). b) In stratigraphic settings continuous BSRs form when the geological environment is more homogeneous while discontinuous BSRs form when fluid flow is happening through discrete permeable layers. c) In venting settings, there is vertical fluid flow through the chimney-like

structures in the subsurface feeding the hydrate-gas system and causing the formation of continuous BSRs.

3.4 Clustered BSRs and paleochannels

Portnov et al. (2019) suggested that clustered BSRs are more commonly associated with coarse-grained sediments. In this study we also observe that twenty-one out of twenty-seven clustered BSR zones are associated with paleochannels (Z-1, 3, 4, 9, GC-955, 42, 45, 46, 47, 50, 55, 57, 58, 59, 62, 63, 65, 66, 67, 69, Orca). These numbers indicate that in the Gulf of Mexico the clustered BSRs are typically associated with the coarser-grained sediments. Figure 10 shows an example of a clustered BSR in Zone-67 associated with a paleochannel.

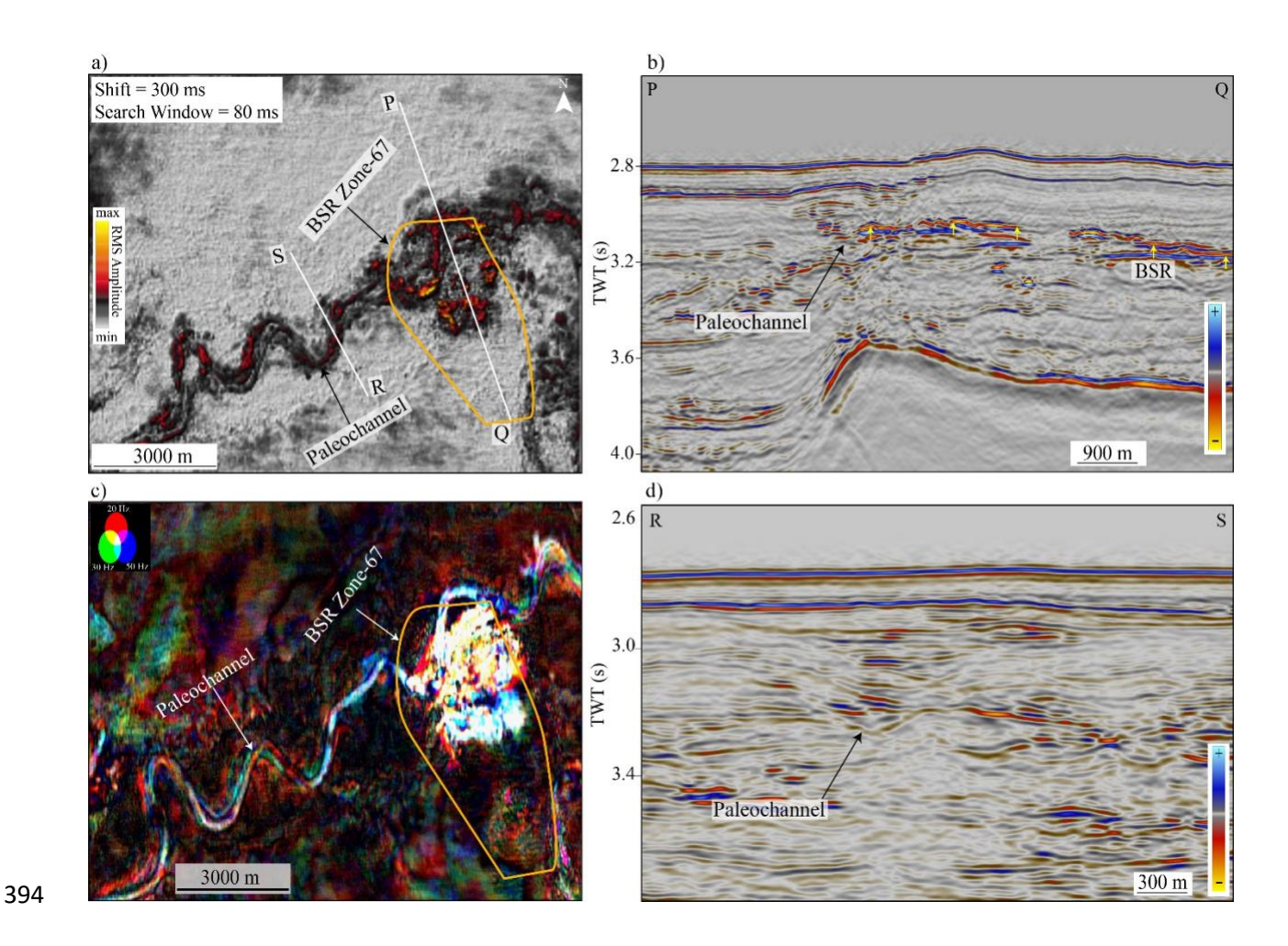


Figure 10: A clustered BSR in Zone-67 associated with a paleochannel. a) RMS amplitude over a reference surface 300 ms below the seafloor. A clear paleochannel is observed with anomalous high amplitudes crossing BSR Zone-67. b) An arbitrary seismic cross section PQ (location shown in Fig 10a) across BSR Zone-67 showing clustered BSR and paleochannel signatures. c) Spectral decomposition (Partyka et al., 2001) delineating a paleochannel feature. d) A seismic profile across the paleochannel showing the channel away from the BSR zone.

3.5 Further implications

Mapping BSRs is essential to identifying hydrate prospects. In the Gulf of Mexico, all gas hydrate systems further explored with scientific ocean drilling were initially identified based on seismic data analysis (McConnell and Kendall, 2002; Ruppel et al., 2008). In particular, clustered

and discontinuous BSRs have been associated with high-saturation gas hydrate in sand and silt-rich reservoirs. For example, GC-955 and Perdido (Figure 1) are two locations where drilling into clustered BSRs revealed high saturated gas hydrate (Flemings et al., 2020; Portnov et al., 2019). Drilling a discontinuous BSR in the Terrebonne basin also confirmed the presence of high saturation hydrate in multiple sand rich reservoirs (Frye et al., 2012). Therefore, our work provides new locations for potential hydrate exploration and production.

405

406

407

408

409

410

411

412

413

414

415

416

417

418

419

420

421

422

423

424

425

426

427

The updip edge of hydrate stability is a climatically sensitive area where gas hydrate can dissociate and methane can leak into the water column (Ruppel and Kessler, 2017). In several locations BSRs are observed near the upper shelf, pinching out near the updip edge of the HSZ (Berndt et al., 2022; Chand et al., 2012; Ketzer et al., 2020). However, it is still unclear how frequently BSRs occur at the updip edge. In this study, we analyzed seismic data across ~1,000 km near the updip edge of hydrate stability on the northern Gulf of Mexico slope and observed only two BSR zones (Zone-28 and Zone-44) (Figure 6). We conclude that at least for the northern Gulf of Mexico, BSR occurrence at the updip edge is uncommon. Whether or not this can be translated to other continental slopes is not clear, and it requires similar-scale geophysical analyses in other regions. One similar study by Mosher (2011) was done on the Canadian Atlantic Margin and analyzed ~2,000 km of 2D and 3D seismic data close to the updip edge of hydrate stability. Mosher (2011) found no BSRs at the updip edge of hydrate stability, though he did not highlight this fact. Alternatively, BSRs at the updip edge of hydrate stability may occur more commonly than in the Gulf of Mexico, but the geologic environment of the Gulf of Mexico does not allow the formation of BSRs at the updip edge of the HSZ. In the Gulf of Mexico, salt tectonics has deformed many near-seafloor sedimentary systems, which may allow free gas to vent directly into the water column instead of trapping gas at the base of the HSZ and forming a BSR.

4. Conclusion

We map and characterize BSRs across the East Breaks, Garden Banks, Green Canyon, Atwater Valley and Mississippi Canyon protraction areas in the northern Gulf of Mexico. Our new BSR catalog includes 74 zones classified by type (continuous, discontinuous, and clustered), geological setting (structural, stratigraphic and venting), and size.

We find that discontinuous BSRs are the most common across the northern Gulf of Mexico. Discontinuous BSRs most often occur in structural settings, created by shallow sediment deformation due to salt tectonics. Clustered BSR systems are also found in structural settings, but they are less common (only 13%) in the Gulf of Mexico. Nonetheless, most clustered BSR zones are associated with paleochannels, indicating that clustered BSRs may occur more frequently in association with coarser-grained sediments. Continuous BSRs are mostly observed within stratigraphic and venting settings. Relatively homogeneous hydrate distribution and laterally

continuous sediments are likely causes for continuous BSRs in stratigraphic settings. Continuous

BSRs in venting setting likely result from laterally focused fluid flow beneath the hydrate stability

Data availability

zone.

- Seismic data are available at the National Archive of Marine Seismic Survey (NAMSS)
- 445 (https://walrus.wr.usgs.gov/namss/search/)

Declaration of competing interest

The authors declare that they have no known competing financial interests or personal relationships that could have appeared to influence the work reported in this paper.

Acknowledgements

The authors would like to acknowledge U.S. Bureau of Ocean Energy Management (BOEM) Award numbers 140M0119P0041, and 140M0122P0017 and National Science Foundation (NSF) award number 1752882 for funding and supporting this work. We sincerely thank the United States Geological Survey (USGS) for preserving the seismic data at the National Archive of Marine Seismic Survey (NAMSS) and making it available in the public domain. We also thank Schlumberger for providing Petrel software to Ohio State University.

Disclaimer

This report was prepared as an account of work sponsored by an agency of the United States government. Neither the United States government nor any agency thereof nor any of their employees make any warranty, express or implied, or assume any legal liability or responsibility for the accuracy, completeness, or usefulness of any information, apparatus, product, or process disclosed, or represent that its use would not infringe privately owned rights. Reference herein to any specific commercial product, process, or service by trade name, trademark, manufacturer, or otherwise does not necessarily constitute or imply its endorsement, recommendation, or favoring by the United States government or any agency thereof. The views and opinions of authors expressed herein do not necessarily state or reflect those of the United States government or any agency thereof.

References:

Anees, A., Shi, W., Ashraf, U., Xu, Q., 2019. Channel identification using 3D seismic attributes and well logging in lower Shihezi Formation of Hangjinqi area, northern Ordos Basin, China. J. Appl. Geophys. 163, 139–150. https://doi.org/10.1016/j.jappgeo.2019.02.015

- Berndt, C., Chi, W.C., Jegen, M., Lebas, E., Crutchley, G., Muff, S., Hölz, S., Sommer, M., Lin,
- S., Liu, C.S., Lin, A.T., Klaeschen, D., Klaucke, I., Chen, L., Hsu, H.H., Kunath, P., Elger,
- J., McIntosh, K.D., Feseker, T., 2019. Tectonic Controls on Gas Hydrate Distribution Off
- 474 SW Taiwan. J. Geophys. Res. Solid Earth 124, 1164–1184.
- 475 https://doi.org/10.1029/2018JB016213
- Berndt, C., Davies, R., Li, A., Yang, J., 2022. Insights into Gas Hydrate Dynamics from 3D
- Seismic Data, Offshore Mauritania, in: World Atlas of Submarine Gas Hydrates in
- 478 Continental Margins. Springer International Publishing, Cham, pp. 323–329.
- 479 https://doi.org/10.1007/978-3-030-81186-0_27
- Boswell, R., Collett, T.S., 2011. Current perspectives on gas hydrate resources. Energy Environ.
- 481 Sci. 4, 1206–1215. https://doi.org/10.1039/c0ee00203h
- Boswell, R., Collett, T.S., Frye, M., Shedd, W., McConnell, D.R., Shelander, D., 2012.
- Subsurface gas hydrates in the northern Gulf of Mexico. Mar. Pet. Geol. 34, 4–30.
- https://doi.org/10.1016/j.marpetgeo.2011.10.003
- Boswell, R., Shelander, D., Lee, M., Latham, T., Collett, T., Guerin, G., Moridis, G., Reagan,
- 486 M., Goldberg, D., 2009. Occurrence of gas hydrate in Oligocene Frio sand: Alaminos
- Canyon Block 818: Northern Gulf of Mexico. Mar. Pet. Geol. 26, 1499–1512.
- 488 https://doi.org/10.1016/j.marpetgeo.2009.03.005
- Boswell, R., Shipp, C., Reichel, T., Shelander, D., Saeki, T., Frye, M., Shedd, W., Collett, T.S.,
- McConnell, D.R., 2016. Prospecting for marine gas hydrate resources. Interpretation 4,
- 491 SA13–SA24. https://doi.org/10.1190/INT-2015-0036.1
- Böttner, C., Haeckel, M., Schmidt, M., Berndt, C., Vielstädte, L., Kutsch, J.A., Karstens, J.,

- Weiß, T., 2020. Greenhouse gas emissions from marine decommissioned hydrocarbon
- wells: leakage detection, monitoring and mitigation strategies. Int. J. Greenh. Gas Control
- 495 100, 103119. https://doi.org/10.1016/j.ijggc.2020.103119
- Brooks, J.M., Cox, H.B., Bryant, W.R., Kennicutt, M.C., Mann, R.G., McDonald, T.J., 1986.
- Association of gas hydrates and oil seepage in the Gulf of Mexico. Org. Geochem. 10, 221-
- 498 234. https://doi.org/10.1016/0146-6380(86)90025-2
- Brooks, J.M., Kennicutt, M.C., Fay, R.R., McDonald, T.J., Sassen, R., 1984. Thermogenic Gas
- Hydrates in the Gulf of Mexico. Science (80-.). 225, 409–411.
- Bünz, S., Polyanov, S., Vadakkepuliyambatta, S., Consolaro, C., Mienert, J., 2012. Active gas
- venting through hydrate-bearing sediments on the Vestnesa Ridge, offshore W-Svalbard.
- 503 Mar. Geol. 332–334, 189–197. https://doi.org/10.1016/j.margeo.2012.09.012
- Chand, S., Thorsnes, T., Rise, L., Brunstad, H., Stoddart, D., Bøe, R., Lågstad, P., Svolsbru, T.,
- 505 2012. Multiple episodes of fluid flow in the SW Barents Sea (Loppa High) evidenced by
- gas flares, pockmarks and gas hydrate accumulation. Earth Planet. Sci. Lett. 331–332, 305–
- 507 314. https://doi.org/10.1016/j.epsl.2012.03.021
- 508 Chun, J.-H., Bahk, J.-J., Um, I.-K., 2022. Ulleung Basin Gas Hydrate Drilling Expeditions,
- Korea: Lithologic Characteristics of Gas Hydrate-Bearing Sediments, in: World Atlas of
- Submarine Gas Hydrates in Continental Margins. Springer International Publishing, Cham,
- pp. 155–161. https://doi.org/10.1007/978-3-030-81186-0_12
- Dewangan, P., Sriram, G., Kumar, A., Mazumdar, A., Peketi, A., Mahale, V., Reddy, S.S.C.,
- Babu, A., 2021. Widespread occurrence of methane seeps in deep-water regions of Krishna-
- Godavari basin, Bay of Bengal. Mar. Pet. Geol. 124, 104783.

https://doi.org/10.1016/j.marpetgeo.2020.104783 515 Dickens, G.R., 2003. Rethinking the global carbon cycle with a large, dynamic and microbially 516 517 mediated gas hydrate capacitor. Earth Planet. Sci. Lett. 213, 169–183. 518 https://doi.org/10.1016/S0012-821X(03)00325-X Expedition 308 Scientists, 2006a. Site U1319, Proc. IODP, 308: College Station TX (Integrated 519 Ocean Drilling Program Management International, Inc.). 520 https://doi.org/10.2204/iodp.proc.308.103.2006 521 522 Expedition 308 Scientists, 2006b. Site U1320, in: Proc. IODP, 308: College Station TX (Integrated Ocean Drilling Program Management International, Inc.). 523 https://doi.org/10.2204/iodp.proc.308.104.2006 524 Flemings, P.B., Phillips, S.C., Boswell, R., Collett, T.S., Cook, A.E., Dong, T., Frye, M., 525 Goldberg, D.S., Guerin, G., Holland, M.E., Jang, J., Meazell, K., Morrison, J., O'Connell, 526 J.I., Petrou, E.G., Pettigrew, T., Polito, P.J., Portnov, A., Santra, M., Schultheiss, P.J., Seol, 527 Y., Shedd, W., Solomon, E.A., Thomas, C.M., Waite, W.F., You, K., 2020. Pressure coring 528 a Gulf of Mexico deep-water turbidite gas hydrate reservoir: Initial results from the 529 University of Texas-Gulf of Mexico 2-1 (UT-GOM2-1) Hydrate Pressure Coring 530 Expedition. Am. Assoc. Pet. Geol. Bull. 104, 1847–1876. 531 https://doi.org/10.1306/05212019052 532 Fraser, D.R.A., Gorman, A.R., Pecher, I.A., Crutchley, G.J., Henrys, S.A., 2016. Gas hydrate 533 accumulations related to focused fluid flow in the Pegasus Basin, southern Hikurangi 534 535 Margin, New Zealand. Mar. Pet. Geol. 77, 399-408. https://doi.org/10.1016/j.marpetgeo.2016.06.025 536

- 537 Frye, M., 2008. Preliminary evaluation of in-place gas hydrate resources: Gulf of Mexico Outer
- Continental Shelf. OCS Rep. MMS 94.
- Frye, M., Shedd, W., Boswell, R., 2012. Gas hydrate resource potential in the Terrebonne Basin,
- Northern Gulf of Mexico. Mar. Pet. Geol. 34, 150–168.
- 541 https://doi.org/10.1016/j.marpetgeo.2011.08.001
- Galloway, W.E., 2008. Chapter 15 Depositional Evolution of the Gulf of Mexico Sedimentary
- Basin, Sedimentary Basins of the World. Elsevier. https://doi.org/10.1016/S1874-
- 544 5997(08)00015-4
- Gullapalli, S., Dewangan, P., Kumar, A., Dakara, G., Mishra, C.K., 2019. Seismic evidence of
- free gas migration through the gas hydrate stability zone (GHSZ) and active methane seep
- in Krishna-Godavari offshore basin. Mar. Pet. Geol. 110, 695–705.
- 548 https://doi.org/10.1016/j.marpetgeo.2019.07.052
- Haines, S.S., Hart, P., Shedd, W.W., Frye, M., 2014. Seismic investigation of gas hydrates in the
- Gulf of Mexico: 2013 multi-component and high-resolution 2D acquisition at GC955 and
- WR313. Proc. Annu. Offshore Technol. Conf. 4, 2549–2566.
- 552 https://doi.org/10.4043/25318-ms
- Haines, S.S., Hart, P.E., Collett, T.S., Shedd, W., Frye, M., Weimer, P., Boswell, R., 2017. High-
- resolution seismic characterization of the gas and gas hydrate system at Green Canyon 955,
- 555 Gulf of Mexico, USA. Mar. Pet. Geol. 82, 220–237.
- https://doi.org/10.1016/j.marpetgeo.2017.01.029
- Hillman, J.I.T., Cook, A.E., Daigle, H., Nole, M., Malinverno, A., Meazell, K., Flemings, P.B.,
- 558 2017a. Gas hydrate reservoirs and gas migration mechanisms in the Terrebonne Basin, Gulf

of Mexico. Mar. Pet. Geol. 86, 1357–1373. https://doi.org/10.1016/j.marpetgeo.2017.07.029 559 Hillman, J.I.T., Cook, A.E., Sawyer, D.E., Küçük, H.M., Goldberg, D.S., 2017b. The character 560 561 and amplitude of 'discontinuous' bottom-simulating reflections in marine seismic data. 562 Earth Planet. Sci. Lett. 459, 157–169. https://doi.org/10.1016/j.epsl.2016.10.058 Holder, G.D., Malone, R.D., Lawson, W.F., 1987. Effects of Gas Composition and Geothermal 563 Properties on the Thickness and Depth of Natural-Gas-Hydrate Zones. JPT, J. Pet. Technol. 564 39, 1147–1152. https://doi.org/10.2118/13595-PA 565 566 Hornbach, M.J., Saffer, D.M., Holbrook, W.S., Van Avendonk, H.J.A., Gorman, A.R., 2008. Three-dimensional seismic imaging of the Blake Ridge methane hydrate province: Evidence 567 for large, concentrated zones of gas hydrate and morphologically driven advection. J. 568 Geophys. Res. Solid Earth 113, 1–15. https://doi.org/10.1029/2007JB005392 569 Hyndman, R.D., Spence, G.D., 1992. A seismic study of methane hydrate marine bottom 570 simulating reflectors. J. Geophys. Res. 97, 6683–6698. https://doi.org/10.1029/92JB00234 571 Ketzer, M., Praeg, D., Rodrigues, L.F., Augustin, A., Pivel, M.A.G., Rahmati-Abkenar, M., 572 Miller, D.J., Viana, A.R., Cupertino, J.A., 2020. Gas hydrate dissociation linked to 573 contemporary ocean warming in the southern hemisphere. Nat. Commun. 11. 574 https://doi.org/10.1038/s41467-020-17289-z 575 Kramer, K. V., Shedd, W.W., 2017. A 1.4-billion-pixel map of the Gulf of Mexico seafloor. Eos 576 (United States). https://doi.org/10.1029/2017eo073557 577 Leslie, S.C., Mann, P., 2022. Distribution and Character of Bottom Simulating Reflections in the 578 Western Caribbean Offshore Guajira Peninsula, Colombia, in: World Atlas of Submarine 579

Gas Hydrates in Continental Margins. Springer International Publishing, Cham, pp. 333– 580 341. https://doi.org/10.1007/978-3-030-81186-0 28 581 Lin, L.-F., Liu, C.-S., Berndt, C., Hsu, H.-H., Wang, Y., Chen, S.-C., 2022. Gas Hydrate and 582 583 Fluid-Related Seismic Indicators Across the Passive and Active Margins off SW Taiwan, in: World Atlas of Submarine Gas Hydrates in Continental Margins. Springer International 584 Publishing, Cham, pp. 173–181. https://doi.org/10.1007/978-3-030-81186-0 14 585 Lindsey, J.P., 1989. The Fresnel zone and its interpetive significance. Lead. Edge 8, 33–39. 586 587 https://doi.org/10.1190/1.1439575 Liu, X., Flemings, P.B., 2007. Dynamic multiphase flow model of hydrate formation in marine 588 sediments. J. Geophys. Res. Solid Earth 112. https://doi.org/10.1029/2005JB004227 589 Majumdar, U., Cook, A.E., Scharenberg, M., Burchwell, A., Ismail, S., Frye, M., Shedd, W., 590 2017. Semi-quantitative gas hydrate assessment from petroleum industry well logs in the 591 northern Gulf of Mexico. Mar. Pet. Geol. 85, 233–241. 592 https://doi.org/10.1016/j.marpetgeo.2017.05.009 593 Malinverno, A., 2010. Marine gas hydrates in thin sand layers that soak up microbial methane. 594 Earth Planet. Sci. Lett. 292, 399–408. https://doi.org/10.1016/j.epsl.2010.02.008 595 Malinverno, A., Goldberg, D.S., 2015. Testing short-range migration of microbial methane as a 596 hydrate formation mechanism: Results from Andaman Sea and Kumano Basin drill sites 597 and global implications. Earth Planet. Sci. Lett. 422, 105–114. 598 https://doi.org/10.1016/j.epsl.2015.04.019 599

Maslin, M., Owen, M., Day, S., Long, D., 2004. Linking continental-slope failures and climate

- change: Testing the clathrate gun hypothesis. Geology 32, 53–56.
- 602 https://doi.org/10.1130/G20114.1
- McConnell, D.R., Collett, T.S., Boswell, R., Frye, M.C., Shedd, W.W., Dufrene, R., Godfriaux,
- P., Mrozewski, S., Guerin, G., Cook, A., Jones, E., 2010. Gulf of Mexico gas hydrate joint
- industry project leg II: Initial results from the Green Canyon 955 site. Proc. Annu. Offshore
- Technol. Conf. 3, 2148–2161. https://doi.org/10.2523/20801-ms
- McConnell, D.R., Kendall, B.A., 2002. Images of the Base of Gas Hydrate Stability, Northwest
- Walker Ridge, Gulf of Mexico. Proc. Annu. Offshore Technol. Conf. 1009–1018.
- 609 https://doi.org/10.4043/14103-ms
- McIver, R.D., 1982. Role of naturally occurring gas hydrates in sediment transport. Am. Assoc.
- Pet. Geol. Bull. 66, 789–792. https://doi.org/10.1306/03b5a318-16d1-11d7-
- 612 8645000102c1865d
- Milkov, A. V., Dickens, G.R., Claypool, G.E., Lee, Y.J., Borowski, W.S., Torres, M.E., Xu, W.,
- Tomaru, H., Tréhu, A.M., Schultheiss, P., 2004. Co-existence of gas hydrate, free gas, and
- brine within the regional gas hydrate stability zone at Hydrate Ridge (Oregon margin):
- Evidence from prolonged degassing of a pressurized core. Earth Planet. Sci. Lett. 222, 829–
- 617 843. https://doi.org/10.1016/j.epsl.2004.03.028
- Milkov, A. V., Sassen, R., 2002. Economic geology of offshore gas hydrate accumulations and
- provinces. Mar. Pet. Geol. 19, 1–11. https://doi.org/10.1016/S0264-8172(01)00047-2
- Milkov, A. V, Sassen, R., 2001. Estimate of gas hydrate resource, northwestern Gulf of Mexico
- continental slope. Mar. Geol. 179, 71–83. https://doi.org/10.1016/S0025-3227(01)00192-X

- Neurauter, T.W., Bryant, W.R., 1990. Seismic expression of sedimentary volcanism on the
- 623 continental slope, northern Gulf of Mexico. Geo-Marine Lett. 10, 225–231.
- https://doi.org/10.1007/BF02431069
- Nole, M., Daigle, H., Cook, A.E., Hillman, J.I.T., Malinverno, A., 2017. Linking basin-scale and
- pore-scale gas hydrate distribution patterns in diffusion-dominated marine hydrate systems.
- Geochemistry, Geophys. Geosystems 18, 653–675. https://doi.org/10.1002/2016GC006662
- Nole, M., Daigle, H., Cook, A.E., Malinverno, A., Flemings, P.B., 2018. Burial-driven methane
- recycling in marine gas hydrate systems. Earth Planet. Sci. Lett. 499, 197–204.
- https://doi.org/10.1016/j.epsl.2018.07.036
- Partyka, G.A., Bush, M.D., Garossino, P.G.A., Gutowski, P.R., 2001. Spectral Decomposition,
- in: Spectral Computations for Bounded Operators. Chapman and Hall/CRC, pp. 19–86.
- https://doi.org/10.1201/9781420035827-3
- Paull, C.K., Matsumoto, R., Wallace, P.J., 1996. Shipboard scientific party, in: Proceedings of
- the Ocean Drilling Program. pp. 99–318.
- Paull, C.K., Ussler, W., Dillon, W.P., 1991. Is the extent of glaciation limited by marine gas-
- hydrates? Geophys. Res. Lett. 18, 432–434. https://doi.org/10.1029/91GL00351
- Paull, C.K., Ussler, W., Lorenson, T., Winters, W., Dougherty, J., 2005. Geochemical constraints
- on the distribution of gas hydrates in the Gulf of Mexico. Geo-Marine Lett. 25, 273–280.
- 640 https://doi.org/10.1007/s00367-005-0001-3
- Petersen, C.J., Papenberg, C., Klaeschen, D., 2007. Local seismic quantification of gas hydrates
- and BSR characterization from multi-frequency OBS data at northern Hydrate Ridge. Earth

- Planet. Sci. Lett. 255, 414–431. https://doi.org/10.1016/j.epsl.2007.01.002
- Portnov, A., Cook, A.E., Sawyer, D.E., 2022. Bottom Simulating Reflections and Seismic Phase
- Reversals in the Gulf of Mexico, in: World Atlas of Submarine Gas Hydrates in Continental
- Margins. Springer International Publishing, Cham, pp. 315–322.
- 647 https://doi.org/10.1007/978-3-030-81186-0 26
- Portnov, A., Cook, A.E., Sawyer, D.E., Yang, C., Hillman, J.I.T., Waite, W.F., 2019. Clustered
- BSRs: Evidence for gas hydrate-bearing turbidite complexes in folded regions, example
- from the Perdido Fold Belt, northern Gulf of Mexico. Earth Planet. Sci. Lett. 528, 115843.
- https://doi.org/10.1016/j.epsl.2019.115843
- Portnov, A., Cook, A.E., Vadakkepuliyambatta, S., 2021. Diverse gas composition controls the
- Moby-Dick gas hydrate system in the Gulf of Mexico. Geology 49, 1446–1451.
- https://doi.org/10.1130/g49310.1
- Portnov, A., Santra, M., Cook, A.E., Sawyer, D.E., 2020. The Jackalope gas hydrate system in
- the northeastern Gulf of Mexico. Mar. Pet. Geol. 111, 261–278.
- https://doi.org/10.1016/j.marpetgeo.2019.08.036
- Roberts, H.H., Hardage, B.A., Shedd, W.W., Hunt, J., 2006. Seafloor reflectivity An important
- seismic property for interpreting fluid/gas expulsion geology and the presence of gas
- 660 hydrate. Lead. Edge 25, 620–628. https://doi.org/10.1190/1.2202667
- Roesink, J.G., Weimer, P., Bouroullec, R., 2004. Sequence stratigraphy of upper Miocene to
- upper Pliocene sediments of east-central Mississippi Canyon, northern Gulf of Mexico.
- Ruppel, C., Boswell, R., Jones, E., 2008. Scientific results from Gulf of Mexico Gas Hydrates

- Joint Industry Project Leg 1 drilling: Introduction and overview. Mar. Pet. Geol. 25, 819–
- 829. https://doi.org/10.1016/j.marpetgeo.2008.02.007
- Ruppel, C.D., Kessler, J.D., 2017. The interaction of climate change and methane hydrates. Rev.
- Geophys. https://doi.org/10.1002/2016RG000534
- Salvador, A., 1991. Origin and development of the Gulf of Mexico basin, in: The Gulf of Mexico
- Basin. Geological Society of America, U.S.A, pp. 389–444. https://doi.org/10.1130/DNAG-
- 670 GNA-J.389
- Santra, M., Flemings, P.B., Scott, E., Kevin Meazell, P., 2020. Evolution of gas hydrate-bearing
- deep-water channel-levee system in abyssal Gulf of Mexico: Levee growth and
- deformation. Am. Assoc. Pet. Geol. Bull. 104, 1921–1944.
- 674 https://doi.org/10.1306/04251918177
- Sassen, R., Roberts, H.H., Carney, R., Milkov, A. V., DeFreitas, D.A., Lanoil, B., Zhang, C.,
- 676 2004. Free hydrocarbon gas, gas hydrate, and authigenic minerals in chemosynthetic
- communities of the northern Gulf of Mexico continental slope: Relation to microbial
- processes. Chem. Geol. 205, 195–217. https://doi.org/10.1016/j.chemgeo.2003.12.032
- 679 Shakhova, N., Semiletov, I., Leifer, I., Sergienko, V., Salyuk, A., Kosmach, D., Chernykh, D.,
- Stubbs, C., Nicolsky, D., Tumskoy, V., Gustafsson, Ö., 2014. Ebullition and storm-induced
- methane release from the East Siberian Arctic Shelf. Nat. Geosci. 7, 64–70.
- https://doi.org/10.1038/ngeo2007
- 683 Shedd, W., Boswell, R., Frye, M., Godfriaux, P., Kramer, K., 2012. Occurrence and nature of "
- bottom simulating reflectors" in the northern Gulf of Mexico. Mar. Pet. Geol. 34, 31–40.
- https://doi.org/10.1016/j.marpetgeo.2011.08.005

- Shipboard Scientific Party, 1986a. Site 617, in: Initial Reports of the Deep Sea Drilling Project,
- 96. U.S. Government Printing Office. https://doi.org/10.2973/dsdp.proc.96.106.1986
- Shipboard Scientific Party, 1986b. Site 618, in: Initial Reports of the Deep Sea Drilling Project,
- 96. U.S. Government Printing Office. https://doi.org/10.2973/dsdp.proc.96.117.1986
- 690 Shipboard Scientific Party, 1986c. Site 619, Initial Reports of the Deep Sea Drilling Project, 96.
- U.S. Government Printing Office. https://doi.org/10.2973/dsdp.proc.96.116.1986
- Shipley, T.H., 1979. Seismic evidence for widespread possible gas hydrate horizons on
- continental slopes and rises. Am. Assoc. Pet. Geol. Bull. 63, 2204–2213.
- 694 https://doi.org/10.1306/2f91890a-16ce-11d7-8645000102c1865d
- 695 Simonetti, A., Knapp, J.H., Sleeper, K., Lutken, C.B., Macelloni, L., Knapp, C.C., 2013. Spatial
- distribution of gas hydrates from high-resolution seismic and core data, Woolsey Mound,
- Northern Gulf of Mexico. Mar. Pet. Geol. 44, 21–33.
- 698 https://doi.org/10.1016/j.marpetgeo.2013.04.004
- 699 Sloan Jr., E.D., Koh, C.A., 2007. Clathrate hydrates of natural gases. CRC Press.
- Snyder, F., Dutta, N., Hutchinson, D., Hart, P., Lee, M.W., Dugan, B., Ruppel, C., Wood, W.,
- 701 Coffin, R., Evans, R., 2004. Seismic analysis and characterization of gas hydrates in the
- Northern deepwater Gulf od Mexico. AAPG Bull 88, 13.
- Sultan, N., Riboulot, V., Ker, S., Marsset, B., Géli, L., Tary, J.B., Klingelhoefer, F., Voisset, M.,
- Lanfumey, V., Colliat, J.L., Adamy, J., Grimaud, S., 2011. Dynamics of fault-fluid-hydrate
- system around a shale-cored anticline in deepwater Nigeria. J. Geophys. Res. Solid Earth
- 706 116, 1–22. https://doi.org/10.1029/2011JB008218

- Sylvester, Z., Deptuck, M.E., Prather, B.E., Pirmez, C., O'byrne, C., 2012. Seismic Stratigraphy
- of a Shelf-Edge Delta and Linked Submarine Channels in the Northeastern Gulf of Mexico,
- in: Application of the Principles of Seismic Geomorphology to Continental-Slope and Base-
- of-Slope Systems: Case Studies from Seafloor and Near-Seafloor Analogues. SEPM
- 711 (Society for Sedimentary Geology), pp. 31–59. https://doi.org/10.2110/pec.12.99.0031
- 712 Triezenberg, P.J., Hart, P.E., Childs, J.R.C., 2016. National Archive of Marine Seismic Surveys
- 713 (NAMSS): A USGS data website of marine seismic reflection data within the US Exclusive
- Economic Zone (EEZ).". US Geol. Surv. data release 10 F7930R7P.
- Vanneste, M., De Batist, M., Golmshtok, A., Kremlev, A., Versteeg, W., 2001. Multi-frequency
- seismic study of gas hydrate-bearing sediments in Lake Baikal, Siberia. Mar. Geol. 172, 1–
- 717 21. https://doi.org/10.1016/S0025-3227(00)00117-1
- Varona, G.M., Flemings, P.B., Portnov, A., 2023. Hydrate-bearing sands in the Terrebonne
- Basin record the transition from ponded deposition to bypass in the deep-water Gulf of
- 720 Mexico. Mar. Pet. Geol. 151, 106172. https://doi.org/10.1016/j.marpetgeo.2023.106172
- Villinger, H.W., Tréhu, A.M., Grevemeyer, I., 2010. 18. Seafloor Marine Heat Flux
- 722 Measurements and Estimation of Heat Flux from Seismic Observations of Bottom
- Simulating Reflectors. Geophys. Charact. Gas Hydrates 279–300.
- 724 https://doi.org/10.1190/1.9781560802197.ch18
- Wallmann, K., Pinero, E., Burwicz, E., Haeckel, M., Hensen, C., Dale, A., Ruepke, L., 2012.
- The global inventory of methane hydrate in marine sediments: A theoretical approach.
- Energies 5, 2449–2498. https://doi.org/10.3390/en5072449
- Wei, L., Cook, A., You, K., 2022. Methane migration mechanisms for the Green Canyon Block

729 955 gas hydrate reservoir, northern Gulf of Mexico. Am. Assoc. Pet. Geol. Bull. 106, 1005– 1023. https://doi.org/10.1306/06022120134 730 731 Weimer, P., Bouroullec, R., Adson, J., Cossey, S.P.J., 2017. An overview of the petroleum 732 systems of the northern deep-water Gulf of Mexico. Am. Assoc. Pet. Geol. Bull. 101, 941– 993. https://doi.org/10.1306/09011608136 733 Xu, W., Ruppel, C., 1999. Predicting the occurrence, distribution, and evolution of methane gas 734 hydrate in porous marine sediments. J. Geophys. Res. 104, 5081–5095. 735 736 You, K., Flemings, P.B., Malinverno, A., Collett, T.S., Darnell, K., 2019. Mechanisms of Methane Hydrate Formation in Geological Systems. Rev. Geophys. 57, 1146–1196. 737 738 https://doi.org/10.1029/2018RG000638 You, K., Summa, L., Flemings, P., Santra, M., Fang, Y., 2021. Three-Dimensional Free Gas 739 Flow Focuses Basin-Wide Microbial Methane to Concentrated Methane Hydrate Reservoirs 740 in Geological System. J. Geophys. Res. Solid Earth 126, 1–20. 741 https://doi.org/10.1029/2021JB022793 742